Fig. 6 Results of incredible natural abundance double-quantum transfer experiment (INADEQUATE), HMBC, selected NOE correlations (a) and ^{1}H-^{15}N HMBC correlations (b) for compound 3 (AB-CHMINACA 2H-indazole analog)
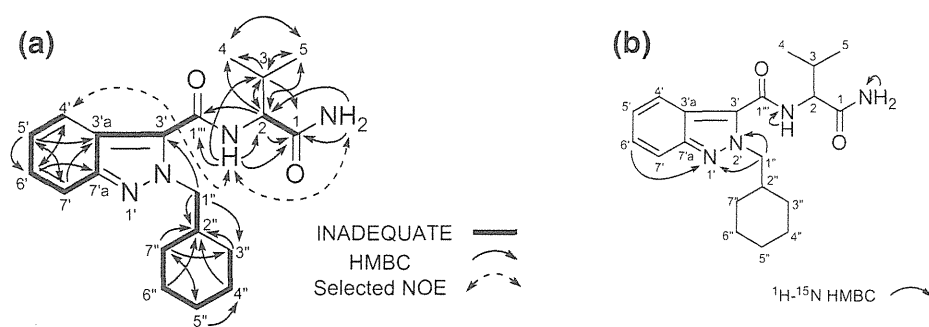

Table 3 ^{15}N NMR data of detected and related compounds

Type	1H-Indazole				2H-Indazole		
Position no.	1-Methyl-1H-indazole[a]	AB-CHMINACA[b]	NNEI indazole analog[c]	Compd. 6[c]	2-Methyl-2H-indazole[a]	Compd. 3[b]	Compd. 4[c]
N-1$'$	−202.8	−191.4	−187.8	−185.5	−91.2	−85.5	−82.7
N-2$'$	−56.6	−62.8	−62.0	−53.0	−161.0	−153.9	−147.4
CONH	–	−273.3	−262.0	–	–	−257.2	−256.5
CONH$_2$	–	−273.3	–	–	–	−274.0	–

^{15}N NMR chemical shifts, which observed in ^{1}H-^{15}N HMBC spectrum, are referenced to the signal of CH$_3$NO$_2$ (δ_N 0.0 ppm)

[a] Ref. [11], recorded in DMSO-d_6
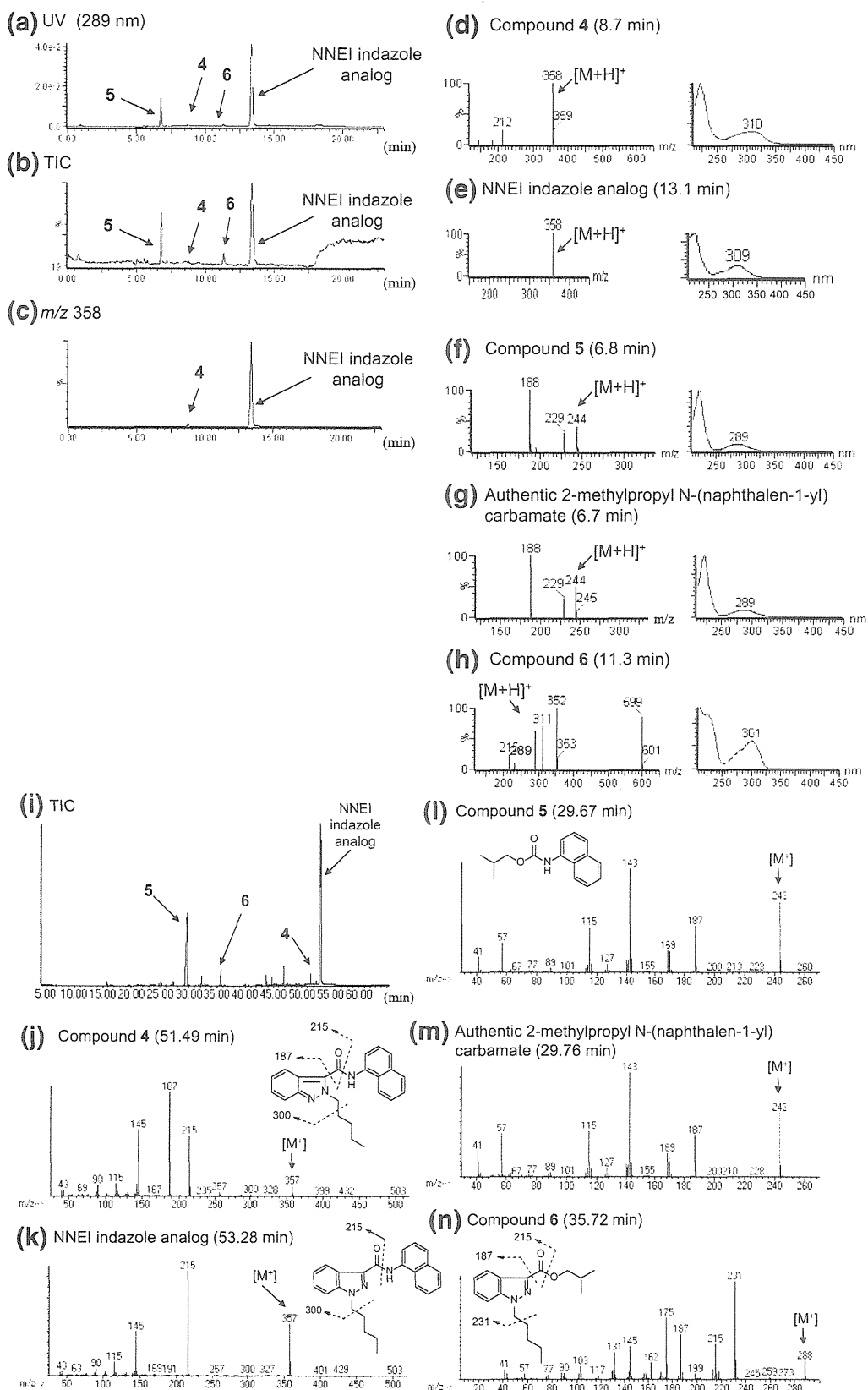
[b] Recorded in DMSO-d_6

[c] Recorded in CDCl$_3$

3 were different from those of the 1H-indazole moiety in 1-methyl-1H-indazole [N-1$'$ (δ_N −202.8) and N-2$'$ (δ_N −56.6)] and AB-CHMINACA [N-1$'$ (δ_N −191.4) and N-2$'$ (δ_N −62.8)], respectively (Table 3; Fig. 1c). However, their shifts of compound 3 were similar to those of 2-methyl-2H-indazole [N-1$'$ (δ_N −91.2) and N-2$'$ (δ_N −161.0)] (Table 3; Fig. 1c) [14]. Therefore, the structure of compound 3 was determined as AB-CHMINACA 2H-indazole analog [N-(1-amino-3-methyl-1-oxobutan-2-yl)-2-(cyclohexylmethyl)-2H-indazole-3-carboxamide] (Fig. 1a).

It was reported that different forms of tautomerism are very common in nitrogen compounds. For indazoles, in most cases the 1H-tautomer is the most stable; however, sometimes several indazoles of the 2H-tautomer can be more stable than 1H-tautomer [14]. The differences in energy between the 1H- and 2H-tautomers were interpreted in terms of substituent effects [14], and we have assumed that the minor component AB-CHMINACA 2H-indazole analog (3) is generated via tautomerization from AB-CHMINACA (1H-indazole). This is the first report of the identification of 2H-indazole isomers of synthetic cannabinoids in illegal products to our knowledge. The chemical characterization, pharmacological activity and toxicological activity of 2H-indazole isomers of synthetic cannabinoids as NPSs have never been reported before.

Identification of unknown peaks 4–6

Three unknown peaks 4, 5, and 6 were detected along with a synthetic cannabinoid NNEI indazole analog in the LC–MS and GC–MS chromatograms for product D (Figs. 7a, b, i, 1b). In the LC–MS and GC–MS analysis, the unknown peak 4 showed a protonated molecular ion signal at m/z 358 [M + H$^+$] (Fig. 7c, d) and a molecular ion signal at m/z 357 [M$^+$] (Fig. 7j). The accurate mass spectrum obtained by LC–QTOF–MS gave an ion signal at m/z 358.1916, suggesting that the protonated molecular formula of compound 4 was C$_{23}$H$_{24}$N$_3$O (calcd. 358.1919). Hence, the presumed molecular formula of compound 4 (C$_{23}$H$_{23}$N$_3$O: 357) was the same as that of NNEI indazole analog. However, the GC–MS and LC–MS spectra patterns and each retention time of both compounds were different (Fig. 7d, e, j, k).

The ^{1}H and ^{13}C NMR spectra (Table 4), HH COSY, HMQC, HMBC and ^{15}N HMBC correlations of compound 4 suggested the presence of N-pentyl-indazole and N-(naphthalen-1-yl)carboxamide moieties (Fig. 8a, b). Therefore, the connectivity of the two moieties (positions 1 and 3$'$) was not observed. On the other hand, the ^{13}C NMR chemical shifts of compound 4 at the C-3$'$ (δc 127.1), C-7$'$ (δc 119.0) and C-7$'$a (δc 147.3) positions were different from those of

🔗 Springer

(a) UV (289 nm)

5   4   6   NNEI indazole analog

(min)

(b) TIC

5   4   6   NNEI indazole analog

(min)

(c) m/z 358

4   NNEI indazole analog

(min)

(d) Compound 4 (8.7 min)

212   358 [M+H]+   359
310   nm

(e) NNEI indazole analog (13.1 min)

358 [M+H]+   309   nm

(f) Compound 5 (6.8 min)

188   229 244 [M+H]+   289   nm

(g) Authentic 2-methylpropyl N-(naphthalen-1-yl) carbamate (6.7 min)

188   229 244 [M+H]+   245   289   nm

(h) Compound 6 (11.3 min)

[M+H]+   352   311   599   353   601   212 289   301   nm

(i) TIC

5   6   4   NNEI indazole analog

5.00 10.00 15.00 20.00 25.00 30.00 35.00 40.00 45.00 50.00 55.00 60.00 (min)

(j) Compound 4 (51.49 min)

215   187   300   [M+]   357   145   215   187   167   43 69 90 115   235 257   300 328   399 432   503   m/z

(k) NNEI indazole analog (53.28 min)

215   215   [M+]   300   357   145   43 63 90 115   159 191   257   300 327   401 429   503   m/z

(l) Compound 5 (29.67 min)

143   [M+]   243   115   187   57   41   67 77 89 101   127   155   169   200 213 228   260   m/z

(m) Authentic 2-methylpropyl N-(naphthalen-1-yl) carbamate (29.76 min)

143   [M+]   243   57   115   187   41   67 77 89 101   127   155   169   200 210 228   m/z

(n) Compound 6 (35.72 min)

215   215   187   231   231   175   187   [M+]   288   41 57   77 90 103 117   131 145   162   139   215   245 259 273   m/z

◀ **Fig. 7** LC–MS and GC–MS analyses of product D. The LC–UV-PDA chromatogram (a), TIC (b) and an extracted-ion chromatogram at m/z 358 (c) are shown, along with the ESI mass and UV spectra of peaks 4 (d), 5 (f), 6 (h), the authentic NNEI indazole analog (e) and the authentic 2-methylpropyl N-(naphthalen-1-yl) carbamate (g). TIC (i) and EI mass spectra of peaks 4 (j), 5 (l), 6 (n), the authentic NNEI indazole analog (k) and the authentic 2-methylpropyl N-(naphthalen-1-yl) carbamate (m) obtained by the GC–MS analysis are also indicated

NNEI indazole analog [C-3′ (δc 137.3), C-7′ (δc 109.4), and C-7′a (δc 141.1)] (Table 4). Comparing the ^{15}N NMR chemical shifts between the two compounds showed that the ^{15}N chemical shifts at the N-1′ (δ$_N$ −82.7) and N-2′ (δ$_N$ −147.4) of the indazole moiety in compound 4 were different from those of the 1H-indazole moiety in NNEI indazole analog [N-1′ (δ$_N$ −187.8) and N-2′ (δ$_N$ −62.0)] (Table 3). However, their shifts of compound 4 were similar to those of 2-methyl-2H-indazole [N-1′ (δ$_N$ −91.2) and N-2′ (δ$_N$ −161.0)] (Table 3) [14]. Therefore, it was revealed that compound 4 has a 2-pentyl-2H-indazole moiety.

We measured the deuterium isotope effect in compound 4 in the same way as that used for compound 2 (Fig. 4c) to determine the connection between the two moieties. The isotope shift values for the ^{13}C NMR signals of this compound are shown in Fig. 8c. The first- to fourth-largest deuterium shifts (0.115, 0.087, 0.048, 0.038 ppm) were observed at the C-1‴, C-1, C-2‴, and C-8‴a positions of the N-(naphthalen-1-yl)-carboxamide moiety. The fifth-largest deuterium shift of 0.029 ppm was attributed to the three-bond deuterium isotope effect of the NH amide proton on the indazole carbon (C-3′). These results suggested that the 2-pentyl-2H-indazole moiety is connected at the 3′-position of the 2H-indazole to the carboxamide (1-CONH). Finally, the structure of compound 4 was determined as NNEI 2H-indazole analog [N-(naphthalen-1-yl)-2-pentyl-2H-indazole-3-carboxamide] (Fig. 1a).

The unknown peak 5 was identified as a 2-methylpropyl N-(naphthalen-1-yl) carbamate (Fig. 7f, l) by direct comparison of the GC–MS and LC–MS data to those of the purchased authentic compound (Fig. 7g, m). This compound has not been reported as any cannabimimetic- or cannabinoid-related substance.

The GC–MS and LC–MS spectra of the unknown peak 6 are shown in Fig. 7h, n. A molecular ion signal of compound 6 was observed at m/z 288 in the GC–MS analysis (Fig. 7n). The accurate mass spectrum obtained by LC–QTOF–MS gave an ion peak at m/z 289.1906, suggesting that the protonated molecular formula of compound 6 was $C_{17}H_{25}N_2O_2$ (calcd. 289.1916). One-dimensional (1D)- and 2D-NMR analyses revealed that compound 6 has isobutyl-carboxylate and N-pentyl-indazole moieties, as shown in Fig. 8d and Table 5. The ^{15}N HMBC correlations of N-1′ with H-6′ and H-2″ (Fig. 8e) and the ^{15}N chemical shifts of
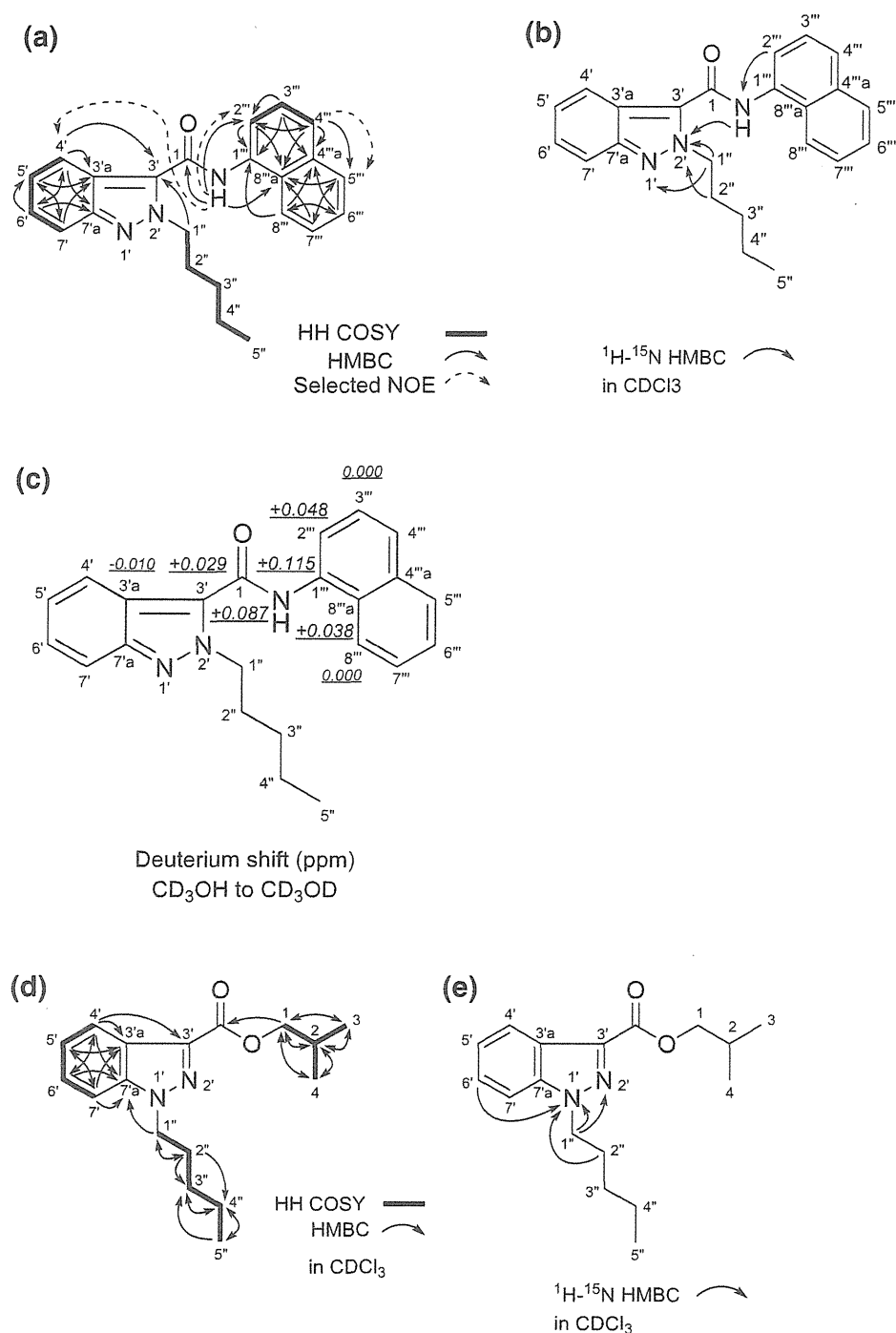
Table 4 NMR data of compound 4 and NNEI indazole analog

No.	NNEI 1H-indazole analog[a] ^{13}C	Compound 4[b]	
		^{13}C	^{1}H
1	160.9	159.0	–
2′	–		–
3′	137.3	127.1	–
3′a	123.0	120.6	–
4′	122.9	118.2	7.94, 1H, d, J = 9.6 Hz, overlapped
5′	122.9	124.9	7.34, 1H, td, J = 7.6, 0.7 Hz
6′	126.9	126.3	7.40, 1H, ddd, J = 7.6, 6.5, 1.0 Hz
7′	109.4	119.0	7.88, 1H, d, J = 8.9 Hz
7′a	141.1	147.3	–
1″	49.6	53.4	4.89, 2H, t, J = 7.2 Hz
2″	29.5	31.0	2.04, 2H, m
3″	29.0	28.9	1.35, 2H, m, overlapped
4″	22.3	22.3	1.35, 2H, m, overlapped
5″	14.0	14.0	0.87, 3H, t, J = 7.2 Hz
1‴	132.4	131.8	–
2‴	119.4	121.1	8.08, 1H, d, J = 7.6 Hz
3‴	126.0	126.2	7.55, 1H, m, overlapped
4‴	125.0	126.6	7.79, 1H, d, J = 8.3 Hz
4‴a	134.2	134.3	–
5‴	128.8	129.0	7.93, 1H, m, overlapped
6‴	125.9	126.8	7.54, 1H, m, overlapped
7‴	126.2	125.8	7.57, 1H, m, overlapped
8‴	120.5	120.4	7.92, 1H, m, overlapped
8‴a	126.7	127.2	–
NH	–	–	8.25, 1H, brs

[a] Recorded in CDCl$_3$ at 800 MHz (^{1}H) and 200 MHz (^{13}C), respectively; data in δ ppm (J in Hz)

[b] Recorded in CDCl$_3$ at 600 MHz (^{1}H) and 150 MHz (^{13}C), respectively; data in δ ppm (J in Hz)

compound 6 at the N-1′ (δ$_N$ −185.5) and N-2′ (δ$_N$ −53.0) of the indazole moiety, which were similar to those of the 1H-indazole moiety in NNEI indazole analog [N-1′ (δ$_N$ −187.8) and N-2′ (δ$_N$ −62.0)], suggested the presence of 1H-indazole (Table 3). No HMBC correlation was observed between the two moieties at position-3′ and ester group of compound 6. However, the major GC–MS fragment ion signal at m/z 187 was probably caused by the cleavage of a bond between the 1H-indazole and the ester group (Fig. 7n). In addition, another fragment ion signal at m/z 215 was probably caused by the cleavage of a bond of the ester group (Fig. 7n). Therefore, the structure of compound 6 was elucidated as isobutyl 1-pentyl-1H-indazole-3-carboxylate (Fig. 1a). Compound 6, which is a novel substance, was not reported to have any pharmacological and toxicological activity.

🖄 Springer

Fig. 8 Results of HH COSY, HMBC, selected NOE correlations (a), ^{1}H-^{15}N HMBC correlations (b) and deuterium-induced isotope shift of NH protons for the ^{13}C NMR signals of compound 4 (NNEI 2H-indazole analog) in CD$_3$OD (c). HH COSY and HMBC correlations (d) and ^{1}H-^{15}N HMBC correlations (e) for compound 6 (isobutyl 1-pentyl-1H-indazole-3-carboxylate), are also shown

(a)

HH COSY
HMBC
Selected NOE

(b)

^{1}H-^{15}N HMBC
in CDCl3

(c)

Deuterium shift (ppm)
CD$_3$OH to CD$_3$OD

(d)

HH COSY
HMBC
in CDCl$_3$

(e)

^{1}H-^{15}N HMBC
in CDCl$_3$

As a result, two major components, i.e., NNEI indazole analog and 2-methylpropyl N-(naphthalene-1-yl) carbamate (5), and three minor components, i.e., isobutyl 1-pentyl-1H-indazole-3-carboxylate (6), NNEI 2H- indazole analog (4) and a presumed 1-pentyl-1H-indazole (elucidated by GC–MS, data not shown) were detected in product D. On the basis of these minor components, we expected the following reaction mechanism for the

Table 5 NMR data of compound **6**

No.	^{13}C	^{1}H
COO	162.9	–
2'	–	–
3'	134.8	–
3'a	123.5	–
4'	122.2	8.17, 1H, d, $J = 8.3$ Hz
5'	122.9	7.29, 1H, t, $J = 8.3$ Hz
6'	126.6	7.41, 1H, t, $J = 8.3$ Hz
7'	109.7	7.46, 1H, d, $J = 8.3$ Hz
7'a	140.5	–
1"	49.9	4.45, 2H, t, $J = 7.3$ Hz
2"	29.6	1.94, 2H, m
3"	28.9	1.29, 2H, m, overlapped
4"	22.3	1.33, 2H, m, overlapped
5"	13.9	0.86, 3H, t, $J = 7.3$ Hz
1	71.0	4.24, 2H, t, $J = 6.4$ Hz
2	27.9	2.19, 1H, m
3/4	19.3	1.05, 6H, d, $J = 6.9$ Hz

Recorded in $CDCl_3$ at 800 MHz (^{1}H) and 200 MHz (^{13}C), respectively; data in δ ppm (J in Hz)

preparation of the major NNEI indazole analog; compound **5** is likely to react with 1-pentyl-1*H*-indazole to yield the major component NNEI indazole analog (path a) and the minor component **6** (path b), as shown in Fig. 9. In addition, the 1*H*- and 2*H*-indazole tautomerism of the starting material or the reaction product accounted for the existence of the minor 2*H*-indazole product (**4**).

Identification of unknown peaks 7 and 8

Unknown peaks **7** and **8** were detected in the LC–MS chromatogram for product E (Fig. 10a, b, e). In the LC–MS chromatogram, the unknown peak **7** at 12.2 min showed a protonated molecular ion signal at m/z 224 ($[M + H]^+$) (Fig. 10c). The accurate mass spectrum obtained by LC–QTOF–MS gave an ion peak at m/z 224.1280, suggesting that the protonated molecular formula of compound **7** was $C_{12}H_{18}NO_3$ (calcd. 224.1287).

The observed ^{1}H and ^{13}C NMR (Table 6), HH COSY, HMQC, HMBC and 1D-NOE revealed that the structure of compound **7** was *N*-hydroxy-3,4-ethylenedioxy-*N*-methylamphetamine (*N*-OH-EDMA), as shown in Fig. 11a. In addition, Noggle et al. [15] reported that *N*-hydroxy-3,4-methylenedioxyamphetamine (*N*-OH-MDA), an analog of *N*-OH-EDMA (**7**), was unstable at high temperatures in a GC–MS analysis, and that *N*-OH-MDA (Fig. 1c) decomposed to MDA (Fig. 1c) [15]. In the present GC–MS TIC chromatogram, peak **7** (*N*-OH-EDMA) was not observed (Fig. 10e). However, the peak of its decomposed compound, which was finally identified as 3,4-ethylenedioxy-*N*-methylamphetamine (3,4-EDMA, Fig. 1b) by direct comparison of the GC–MS data to those of the purchased authentic compound (Fig. 10g), was detected (Fig. 10e, f). No pharmacological information is available for *N*-OH-EDMA (**7**); however, 3,4-EDMA has been reported to stimulate the release of serotonin and dopamine from rat brain synaptosomes at 1 μM [16].

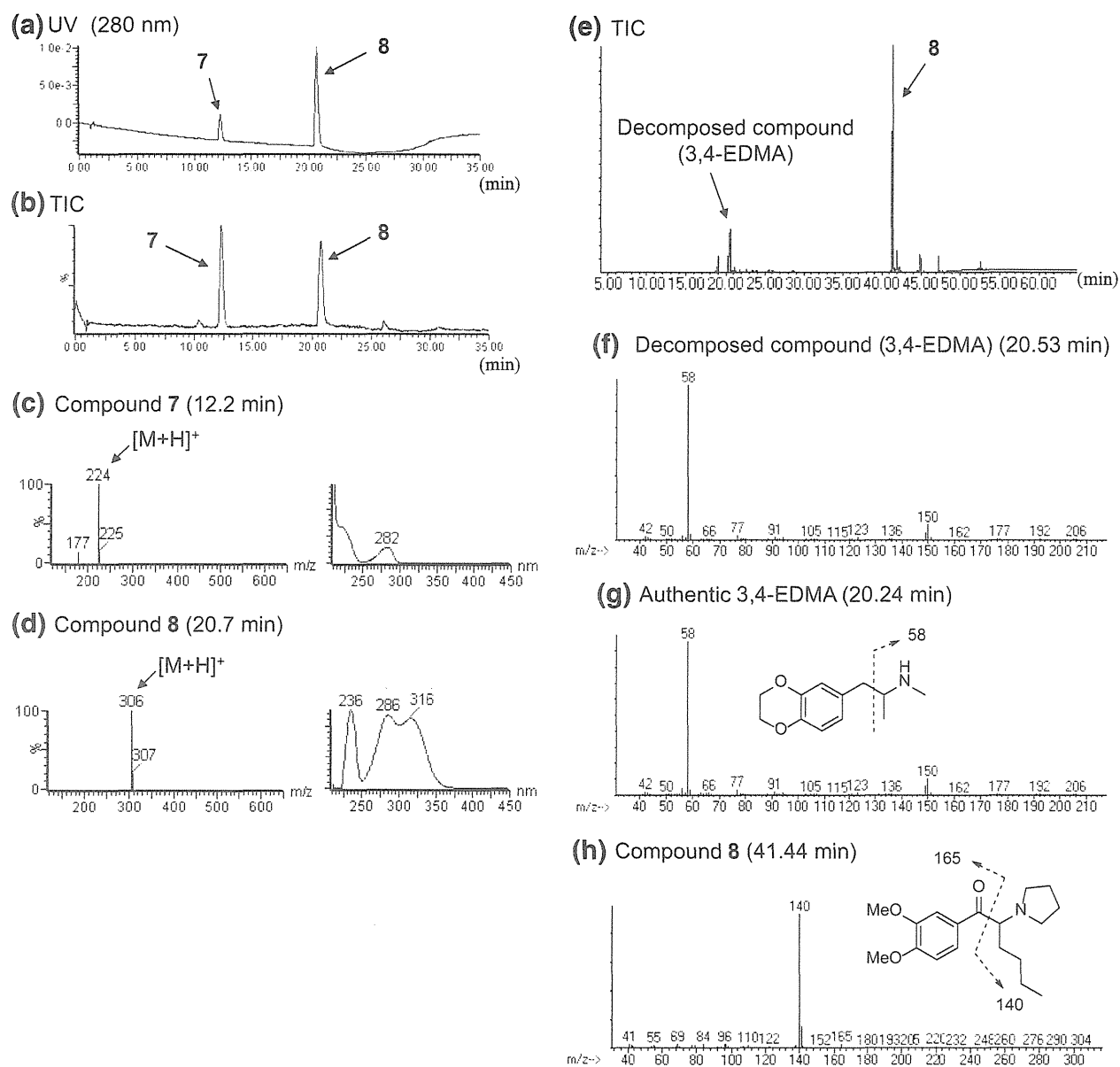The proposed fragment pattern and the presumed structure of peak **8** obtained by the GC–MS analysis

Fig. 9 Possible reaction mechanisms for the preparation of NNEI indazole analog and compound **6**

path a

path b

path a

path b

2-Methylpropyl *N*-(naphthalen-1-yl) carbamate (**5**)
Major component

NNEI indazole analog
Major component

Isobutyl 1-pentyl-1*H*-indazole-3-carboxylate (**6**)
Minor component

1-Pentyl-1*H*-indazole
Minor component

(a) UV (280 nm)

(b) TIC

(c) Compound 7 (12.2 min)

[M+H]$^+$

(d) Compound 8 (20.7 min)

[M+H]$^+$

(e) TIC

Decomposed compound (3,4-EDMA)

8

(f) Decomposed compound (3,4-EDMA) (20.53 min)

(g) Authentic 3,4-EDMA (20.24 min)

(h) Compound 8 (41.44 min)

Fig. 10 LC–MS and GC–MS analyses of product E. The LC–UV-PDA chromatogram (a), TIC (b), ESI mass and UV spectra of peaks 7 (c) and 8 (d) are shown. TIC (e) and EI mass spectra of peaks of

decomposed compound [3,4-ethylenedioxy-N-methylamphetamine (3,4-EDMA)] (f), compound 8 (h) and the authentic 3,4-EDMA (g) obtained by GC–MS analysis are also presented

are shown in Fig. 10h. The LC–MS data revealed that peak 8 gave a protonated ion signal at m/z 306 ([M + H]$^+$) (Fig. 10d). The accurate mass spectrum obtained by LC–QTOF–MS gave an ion peak at m/z 306.2072, suggesting that the protonated molecular

formula of compound 8 was $C_{18}H_{28}NO_3$ (calcd. 306.2069).

The ^{13}C NMR spectrum of compound 8 was similar to a combination of two known cathinone derivatives: an α-pyrrolidinohexanone moiety of α-PHP and a 3,4-

Table 6 NMR data of compound **7**

No.	^{13}C	^1H
1	38.3	2.84, 1H, dd, J = 13.1, 4.5 Hz
		2.26, 1H, dd, J = 13.4, 8.6 Hz
2	64.2	2.67, 1H, m
3	14.1	0.83, 3H, d, J = 6.5 Hz
1′	133.2	–
2′	117.6	6.66, 1H, d, J = 1.7 Hz
3′	142.9	–
4′	141.4	–
5′	116.5	6.71, 1H, d, J = 7.9 Hz
6′	121.9	6.61, 1H, dd, J = 8.3, 1.7 Hz
$-O-(CH_2)_2-O-$	64.0	4.18, 4H, m
	63.9	
N–CH$_3$	44.2	2.46, 3H, s
N–OH	–	7.64, 1H, brs

Recorded at 600 MHz (^1H) and 150 MHz (^{13}C) in DMSO-d_6, respectively; data in δ ppm (J in Hz)

Table 7 NMR data of compound **8**

No.	^{13}C	^1H
1	199.1	–
2	68.7	4.08, 1H, dd, J = 9.3, 4.8 Hz
3	30.0	2.08, 1H, m
		1.83, 1H, m
4	28.9	1.32, 2H, m
5	23.1	1.26, 2H, m
6	14.1	0.78, 3H, t, J = 7.2 Hz
1′	130.6	–
2′	111.9	8.03, 1H, d, J = 1.7 Hz
3′	149.5	–
4′	154.1	–
5′	111.1	7.00, 1H, d, J = 8.6 Hz
6′	123.7	8.15, 1H, dd, J = 8.6, 1.7 Hz
2″/5″	50.7	2.75, 2H, m
		2.64, 2H, m
3″/4″	23.9	1.63, 4H, m
3′-MeO	55.9/55.7	3.78, 3H, s
4′-MeO	55.7/55.9	3.78, 3H, s

Recorded at 600 MHz (^1H) and 150 MHz (^{13}C) in pyridine-d_5, respectively; data in δ ppm (J in Hz)

dimethoxyphenyl moiety of DL-4662 (Table 7) [13]. The observed ^1H and ^{13}C NMR (Table 7), HH COSY, HMQC, HMBC, and 1D-NOE correlations (Fig. 11b) suggested that the structure of compound **8** is dimethoxy-α-pyrrolidinohexanophenone (dimethoxy-α-PHP), as shown in Fig. 1a. The fragment ions at m/z 140 and 165 of compound **8** in the GC–MS spectrum corroborated the structure (Fig. 10h). Compound **8** was detected as a newly distributed designer drug, and its chemical and pharmaceutical data have not been reported. Dimethoxy-α-PHP (**8**) has been controlled as a designated substance (Shitei-Yakubutsu) in Japan since November 2014.

Conclusions

Four synthetic cannabinoids: FDU-PB-22 (**1**), FDU-NNEI (**2**), two 2H-indazole isomers of synthetic cannabinoids, i.e., AB-CHMINACA 2H-indazole analog (**3**) and NNEI 2H-indazole analog (**4**), a phenethylamine derivative N-OH-EDMA (**7**), and a cathinone derivative dimethoxy-α-PHP (**8**) were newly identified in illegal products obtained in Japan. In addition, 2-methylpropyl N-(naphthalen-1-yl) carbamate (**5**) and isobutyl 1-pentyl-1H-indazole-3-carboxylate (**6**), which is probably a by-product in the synthesis of NNEI indazole analog from 1-pentyl-1H-indazole and compound **5** (Fig. 9), were detected. Among them, compounds **3**, **4**, and **6** were detected as minor components; their pharmacological and toxicological properties have never been reported. This appears to be the first report to estimate the synthetic pathway of illegal synthetic cannabinoids on the basis of detailed analytical data of illegal products.
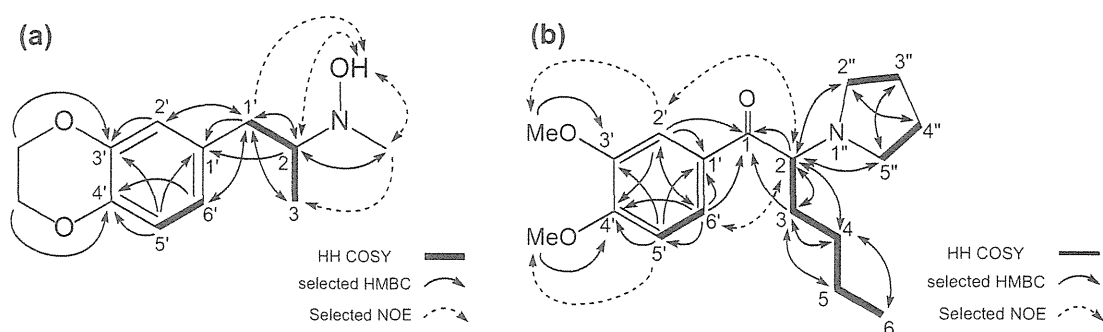

Fig. 11 HH COSY, HMBC, and selected NOE correlations for compound **7** (N-OH-EDMA, a) and for compound **8** (dimethoxy-α-PHP, b)

References

1. EMCDDA (2014) European drug report 2014: trends and developments, May 2014. http://www.emcdda.europa.eu/attachements.cfm/att_228272_EN_TDAT14001ENN.pdf. Accessed Nov 2014
2. EMCDDA–Europol (2013) Annual report on the implementation of Council Decision 2005/387/JHA, July 2014. http://www.emcdda.europa.eu/publications/implementation-reports/2013. Accessed Nov 2014
3. UNODC (2014) 2014 Global synthetic drugs assessment. Amphetamine-type stimulants and new psychoactive substances, May 2014. http://www.unodc.org/documents/scientific/2014_Global_Synthetic_Drugs_Assessment_web.pdf. Accessed May 2014
4. Zuba D, Byrska B (2013) Analysis of the prevalence and coexistence of synthetic cannabinoids in "herbal high" products in Poland. Forensic Toxicol 31:21–30
5. Kikura-Hanajiri R, Uchiyama N, Kawamura M, Goda Y (2013) Changes in the prevalence of synthetic cannabinoids and cathinone derivatives in Japan until early 2012. Forensic Toxicol 31:44–53
6. Chung H, Choi H, Heo S, Kim E, Lee J (2014) Synthetic cannabinoids abused in South Korea: drug identifications by the National Forensic Service from 2009 to June 2013. Forensic Toxicol 32:82–88
7. Kikura-Hanajiri R, Uchiyama N, Kawamura M, Goda Y (2014) Changes in the prevalence of new psychoactive substances before and after the introduction of the generic scheduling of synthetic cannabinoids in Japan. Drug Test Anal 6:832–839
8. Uchiyama N, Matsuda S, Kawamura M, Kikura-Hanajiri R, Goda Y (2014) Identification of two new-type designer drugs, piperazine derivative MT-45 (I-C6) and a synthetic peptide Noopept (GVS-111), with synthetic cannabinoid A-834735, cathinone derivative 4-methoxy-α-PVP and phenethylamine derivative 4-methylbuphedrine from illegal products. Forensic Toxicol 32:9–18
9. Uchiyama N, Shimokawa Y, Matsuda S, Kawamura M, Kikura-Hanajiri R, Goda Y (2014) Two new synthetic cannabinoids, AM-2201 benzimidazole analog (FUBIMINA) and (4-methylpiperazin-1-yl)(1-pentyl-1H-indol-3-yl)methanone (MEPIRAPIM), and three phenethylamine derivatives, 25H-NBOMe 3,4,5-trimethoxybenzyl analog, 25B-NBOMe, and 2C-N-NBOMe, identified in illegal products. Forensic Toxicol 32:105–115
10. Uchiyama N, Matsuda S, Kawamura M, Shimokawa Y, Kikura-Hanajiri R, Aritake K, Urade Y, Goda Y (2014) Characterization of four new designer drugs, 5-chloro-NNEI, NNEI indazole analog, α-PHPP and α-POP, with 11 newly distributed designer drugs in illegal products. Forensic Sci Int 243:1–13
11. Uchiyama N, Kawamura M, Kikura-Hanajiri R, Goda Y (2013) URB-754: a new class of designer drug and 12 synthetic cannabinoids detected in illegal products. Forensic Sci Int 227:21–32
12. Uchiyama N, Matsuda S, Kawamura M, Kikura-Hanajiri R, Goda Y (2013) Two new-type cannabimimetic quinolinyl carboxylates, QUPIC and QUCHIC, two new cannabimimetic carboxamide derivatives, ADB-FUBINACA and ADBICA, and five synthetic cannabinoids detected with a thiophene derivative α-PVT and an opioid receptor agonist AH-7921 identified in illegal products. Forensic Toxicol 31:223–240
13. Uchiyama N, Shimokawa Y, Kawamura M, Kikura-Hanajiri R, Hakamatsuka T (2014) Chemical analysis of a benzofuran derivative, 2-(2-ethylaminopropyl)benzofuran (2-EAPB), eight synthetic cannabinoids, five cathinone derivatives and five other designer drugs newly detected in illegal products. Forensic Toxicol 32:266–281
14. Elguero J, Silva AMS, Tomé AC (2011) Five membered heterocycles: 1,2-azoles. Part 1. Pyrazoles. In: Alvarez-Builla J, Vaquero JJ, Barluenga J (eds) Modern heterocyclic chemistry, vol 2. WileyVCH Verlag, Weinheim, pp 635–725
15. Noggle FT Jr, Clark CR, Valaer AK, DeRuiter J (1988) Liquid chromatographic and mass spectral analysis of N-substituted analogues of 3,4-methylenedioxyamphetamine. J Chromatogr Sci 26:410–417
16. McKenna DJ, Guan X-M, Shulgin AT (1991) 3,4-Methylenedioxyamphetamine (MDA) analogues exhibit differential effects on synaptosomal release of ^{3}H-dopamine and ^{3}H-5-hydroxytryptamine. Pharmacol Biochem Behav 38:505–512

Contents lists available at ScienceDirect

Neuroscience Letters
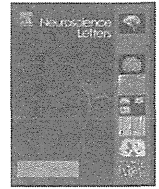
Research article

An inhibitory pathway controlling the gating mechanism of the mouse lateral amygdala revealed by voltage-sensitive dye imaging

CrossMark

Tomomi Fujieda [a,b], Noriko Koganezawa [b], Yoshinori Ide [a], Tomoaki Shirao [b], Yuko Sekino [a,b,*]

[a] Division of Pharmacology, National Institute of Health Sciences, 1-18-1 Kamiyoga, Setagaya-ku, Tokyo 158-8501, Japan
[b] Department of Neurobiology and Behavior, Gunma University Graduate School of Medicine, 3-39-22 Showa-machi, Maebashi, Gunma 371-8511, Japan

HIGHLIGHTS

- EC stimulation induces large and long-lasting hyperpolarizing signals in the La.
- This hyperpolarization is analyzed by VSD imaging spatially and temporally.
- We identify an inhibitory pathway toward the La via the m-ITC.

ARTICLE INFO

ABSTRACT

The lateral amygdala nucleus (La) is known as a gateway for emotional learning that interfaces sensory inputs from the cortex and the thalamus. In the La, inhibitory GABAergic inputs control the strength of sensory inputs and interfere with the initial step of the acquisition of fear memory. In the present study, we investigated the spatial and temporal patterns of the inhibitory responses in mouse La using voltage-sensitive dye imaging. Stimulating the external capsule (EC) induced large and long-lasting hyperpolarizing signals in the La. We focused on these hyperpolarizing signals, revealing the origins of the inhibitory inputs by means of surgical cuts on the possible afferent pathways with four patterns. Isolating the medial branch of EC (ECmed), but not the lateral branch of EC (EClat), from the La strongly suppressed the induction of the hyperpolarization. Interestingly, isolating the ECmed from the caudate putamen did not suppress the hyperpolarization, while the surgical cut of the ECmed fiber tract moderately suppressed it. Glutamatergic antagonists completely suppressed the hyperpolarizing signals induced by the stimulation of EC. When directly stimulating the dorsal, middle or ventral part of the ECmed fiber tract in the presence of glutamatergic antagonists, only the stimulation in the middle part of the ECmed caused hyperpolarization. These data indicate that the GABAergic neurons in the medial intercalated cluster (m-ITC), which receive glutamatergic excitatory input from the ECmed fiber tract, send inhibitory afferents to the La. This pathway might have inhibitory effects on the acquisition of fear memory.

1. Introduction

The amygdala is an important brain structure for emotional behavior and learning [13]. Fear conditioning is a widely-used experimental model to examine emotional and learning processing in animal brains. The lateral amygdala nucleus (La) is known as a

gateway for emotional learning that interfaces sensory inputs from the cortex and the thalamus [14]. Inhibitory circuits are known to control the amygdala's functions, such as acquisition, expression, and extinction of conditioned fear [6,21,22]. Inhibitory inputs to the La control the strength of sensory inputs and interfere with the initial step of the acquisition of fear memory. Two groups of GABAergic neurons in the amygdala are known: local interneurons that are scattered within the local neuropil [17], and intercalated cells organized in clusters (intercalated clusters) surrounding the amygdala complex [15,16,18,20,23,24]. Although inhibitory inputs to the individual principal neurons in the amygdala have been analyzed electrophysiologically [4,26,31,37,38], how sensory inputs

* Corresponding author at: Division of Pharmacology, National Institute of Health Sciences, 1-18-1 Kamiyoga, Setagaya-ku, Tokyo 158-8501, Japan.
Tel.: +81 3 3700 9692; fax: +81 3 3700 1452.
E-mail address: yukos@nihs.go.jp (Y. Sekino).

induce inhibitory responses in the La, and how inhibitory responses propagate in the La, are still unclear because of the technical limitations of patch clamp recording.

Optical imaging techniques overcome these limitations to investigating propagations in a wide range of neuronal interactions, and have been applied in the study of excitatory circuits of several brain regions [7,9,11,12,29,33,34]. In this study, using optical imaging techniques, we investigate neuronal activities in the La, focusing particularly on inhibitory responses. To identify the origins of the inhibitory inputs, we perform various patterns of knife-cut operations of the possible afferent pathways evoking hyperpolarization in the La. In addition, we investigate the effects of glutamatergic antagonists on the inhibitory responses in the La, and show an inhibitory pathway from the medial intercalated cluster (m-ITC) to the La.

2. Materials and methods

2.1. Slice preparation and staining procedure

The experimental protocol was reviewed and approved by the National Institute of Health Sciences (NIHS) in Japan, following the guidelines in the National Research Council's 'Guide for the Care and Use of Laboratory Animals'. All experiments were approved by the NIHS' ethics committee. Male mice (C57BL/6J, 7–22 weeks old, Japan SLC, Inc., Japan) were deeply anesthetized with halothane and quickly decapitated. Coronal slices containing the amygdala complex (400 μm) were prepared using a vibrating microtome (Campden Instruments Ltd., Loughborough, UK) in ice-cold artificial cerebrospinal fluid (ACSF). The ACSF was composed of the following (in mM): 119 NaCl, 2.5 KCl, 1.3 MgSO$_4$, 2.5 CaCl$_2$, 1.0 NaH$_2$PO$_4$, 26.2 NaHCO$_3$, and 11.0 glucose; this was oxygenated with a mixture gas of 95% O$_2$ and 5% CO$_2$ (pH 7.4). The slices were immediately soaked in the oxygenated ACSF containing a voltage-sensitive dye (VSD), di-4-ANEPPS (50 μM, Invitrogen Molecular Probes Inc., Oregon, USA) for 10 s, and then transferred to a filter that absorbed the staining solution and subsequently to another filter that absorbed the normal ACSF for at least an hour before the experiment.

2.2. Experimental apparatus for VSD imaging

An epi-illumination macro zoom fluorescence microscopy (MVX-10 MacroView, Olympus, Japan), a LED light source with a 530 nm center wavelength (LEX2-Green, Brainvision Inc., Tokyo, Japan), a dichroic mirror (560 nm), an emission filter (BP 575–625 nm), and a CMOS imaging device (MiCAM ULTIMA-L, Brainvision Inc., Tokyo) were used for VSD imaging.

The decrease and increase in the fluorescent intensity from the preparation corresponded to the membrane depolarization and hyperpolarization, respectively. Each data acquisition consisted of 1024 images of consecutive frames (1.0 ms/frame). A coaxial needle electrode (TF203-047, Unique Medical Co. Ltd., Tokyo, Japan) was placed on the external capsule (EC). Electrical stimuli with 200-μs duration at various intensities from 15 to 90 μA were delivered at the 100th frame of each acquisition. To analyze the effects of deafferentation on the induction of the hyperpolarization, the stimulus intensity was adjusted to make the peak value of depolarization equal before and after the surgical cut. Methods to calculate optical signals and present images were described in previous papers [11,29,32].

2.3. Surgical cuts of afferent connections to the La

After recording the optical signals at various stimulation intensities, we performed knife-cut operations on the pathways assumed to be involved in the induction of the hyperpolarization in the La.

Four afferent pathways to the La were cut under the macro scope observation, as follows: the La was isolated by the longitudinal cut from: (i) the lateral branch of the EC, (ii) the medial branch of the EC and (iii) the CPu, and by (iv) the transverse cut of ECmed at the dorsal part. For the sham operations, the slices remained intact but the same procedure was carried out. After the surgical cuts, the slices were stored in the recovery chamber at room temperature (at least 1 h).

2.4. Excitation and inhibition values

Images from the 251st–300th frames were stacked and averaged to determine regions of interest (ROIs), which were circles of 8 pixels in diameter. Two ROIs were defined for each experiment. One of the ROIs had the maximal hyperpolarization value in the center spot. The other was adjacent to the first, which had an adequately large hyperpolarization value within the region. For the after-operation analysis, the ROIs were centered on the spots that had the same distances from the position of the stimulating electrode and the EC as the before-operation analysis. The averaged optical signals of the two ROIs were used as representative data.

The excitation (E) value was determined as the largest value among all the values from the first to the 15th frame after electrical stimulation. The inhibition (I) value was determined by averaging 50 frames, from the 251st frame to the 300th frame after the electrical stimulation.

2.5. Statistical analysis

We defined the operation index (OI) as follows: OI = $[I/E]_a/[I/E]_b$, where a: after the operation, b: before the operation. The data were presented as mean ± standard error of the mean (SEM). Normality of the data was tested with the Shapiro–Wilk test, and subsequently one-way ANOVA followed by Dunnett's post-hoc test was carried out. In the pharmacological experiments, inhibition value was statistically analyzed using a paired t-test.

3. Results

3.1. Optical signal propagation after the EC stimulation

The anatomical nomenclatures related to our experiments are shown in Fig. 1A. Each white fiber bundle in the amygdala slice preparation was observed through the macro zoom microscope; thus, the ramifying point of the EC was identified. The La, BLA, and CeA of the amygdala complex were identified in the fluorescent image recorded by the system (Fig. 1B). In Fig. 1C, a typical example of the optical signal propagation is shown in pseudo-color representation. The depolarization started at the stimulation point and spread over the La within 3 ms after the stimulation (0–3 ms). It became stronger in the La and spread over the other regions, the BLA, CPu, and CeA (4–7 ms). Then the depolarization at the dorsal area of the La faded, while growing stronger in the other regions (8–11 ms). Following depolarization, a weak hyperpolarization was first observed in the La; the depolarization remained in the other regions, although it was weakened (12–15 ms). The hyperpolarization grew stronger, and the depolarization in the other regions gradually disappeared (16–19 ms). The hyperpolarization in the La lasted about 600–650 ms (the middle wave in Fig. 1B). The maximal value of the hyperpolarization was observed around 255 ms after the stimulation.

After the hyperpolarization started in the La at the area along the dorsal part of the ECmed (16–19 ms), it spread out in the La during the next 100 ms (20–119 ms), then it spread over the BLA and a narrow part of the CPu along the dorsal part of the ECmed
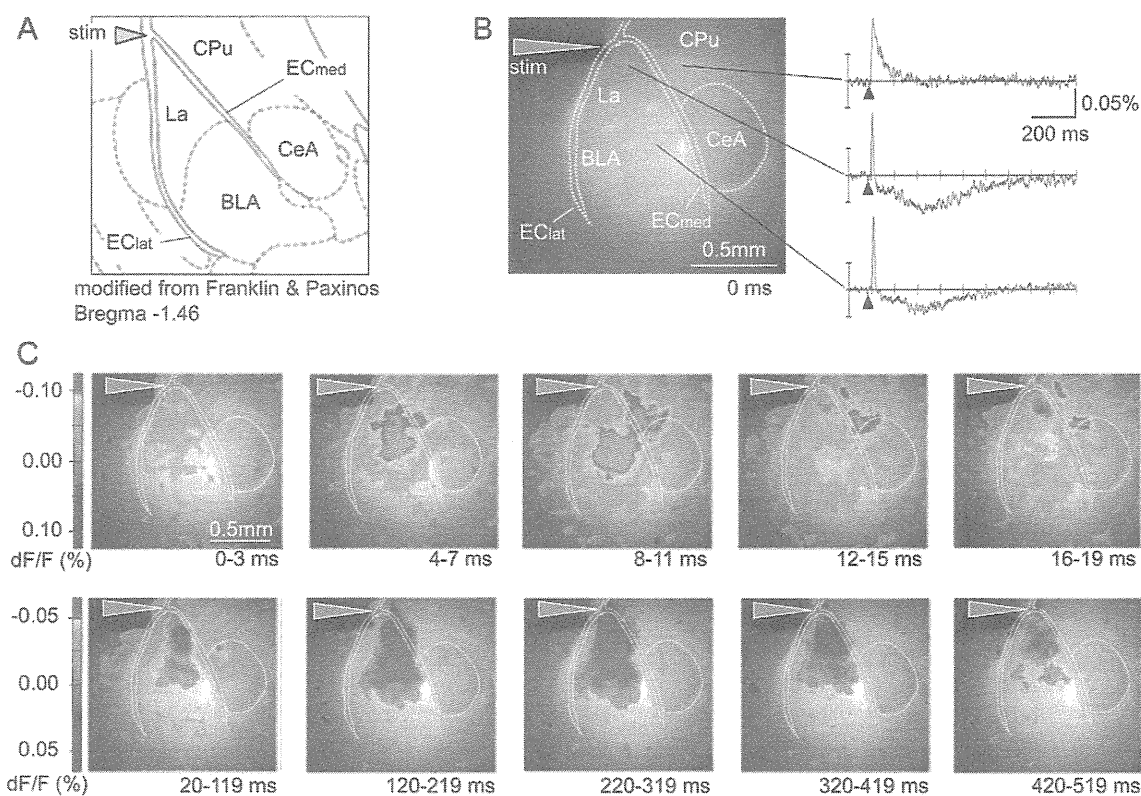
Fig. 1. Optical signal propagation after the EC stimulation.
(A) The modified schematic diagram from the atlas of Franklin and Paxinos (2007) at Bregma −1.46 mm. The arrowhead shows the ramifying point of the external capsule (EC); lateral branch of the external capsule (EClat) and medial branch of the external capsule (ECmed). La – lateral amygdala nucleus; BLA – basolateral amygdala nucleus; CeA – central amygdala nucleus; CPu – caudate putamen. (B) Left, the fluorescence image of VSD-stained coronal slice. Right, a typical example of optical signals in the CPu (in the top wave), La (in the middle wave) and BLA (in the bottom wave). Brown arrowhead, the stimulating site; black arrowhead, the timing of electrical stimulation. (C) Images of optical signal changes produced at the various indicated times after electrical stimulation. In the upper panels, images for 4 frames were stacked to show the spread pattern of depolarization. In the lower panels, images for 100 frames were stacked to show the spread pattern of hyperpolarization.

during the following 100 ms (120–219 ms). The maximal hyperpolarization was observed in the La along the dorsal part of the ECmed from 220 to 319 ms. The strong and long-lasting hyperpolarization was mainly observed in the La (the middle wave in Fig. 1B), while the hyperpolarization in the BLA was weak (the bottom wave). The hyperpolarization was neither observed in the main part of the CPu (the top wave) nor in the CeA, while the depolarization in the CPu lasted longer than in the La and the BLA.

3.2. Effects of the deafferentation on the optical signals

To reveal the afferent pathway responsible for evoking the strong and long-lasting hyperpolarization, effects of the various surgical operations were investigated.

Deafferentation from the EClat to the La did not affect the induction of the strong and long-lasting hyperpolarization in the La (Fig 2A), and there was no significant change in the OI value compared with the sham (Fig. 2E), suggesting that the afferent inputs via the EClat are not involved in the hyperpolarization induced in the La. In contrast, deafferentation from the ECmed to the La strongly reduced the hyperpolarization (Fig. 2B). OI values were also significantly reduced (Fig. 2E). These results suggest that the inputs via the ECmed are involved in the hyperpolarization induced in the La.

Next, to investigate the involvement of inputs from the main part of the CPu, we cut off the input from the CPu to the ECmed. In this experiment, the connections between the ECmed and the La remained. The OI values after deafferentation did not significantly change (Fig. 2C and E), suggesting that the inputs from the CPu are

not involved in the hyperpolarization induced in the La. For further investigation of the inputs via ECmed, a transverse cut at the dorsal part of the ECmed was carried out. As a result, the hyperpolarization was significantly reduced in the La (Fig. 2D). These data suggest that the fibers running along the ECmed were involved in the induction of hyperpolarization.

3.3. Effects of glutamatergic antagonists and the source of the inhibition

Finally, to confirm the details of the inhibitory input source and its properties, the effects of glutamatergic antagonists (6-cyano-7-nitroquinoxaline-2,3-dione (CNQX, 10 μM, TOCRIS), D-(−)-2-amino-5-phosphonopentanoic acid (D-AP5, 50 μM, TOCRIS)) on the inhibitory responses were investigated. The inhibitory responses in the La induced by EC stimulation were statistically significantly reduced after the application of glutamatergic antagonists (Fig. 3A), suggesting that excitatory glutamatergic inputs were involved in the inhibitory response.

We then stimulated several parts along the ECmed in the presence of glutamatergic antagonists (Fig. 3B). Stimulation at the dorsal part of the ECmed did not induce the hyperpolarization (Fig. 3Ba); however, the hyperpolarization could be induced when the middle part of the ECmed was stimulated (Fig. 3Bb). When the electrode moved to the ventral part of the ECmed, weak hyperpolarizing responses were observed (Fig. 3Bc). The magnitude of the hyperpolarization induced by the stimulation at the middle part of the ECmed was statistically significantly larger than that induced by
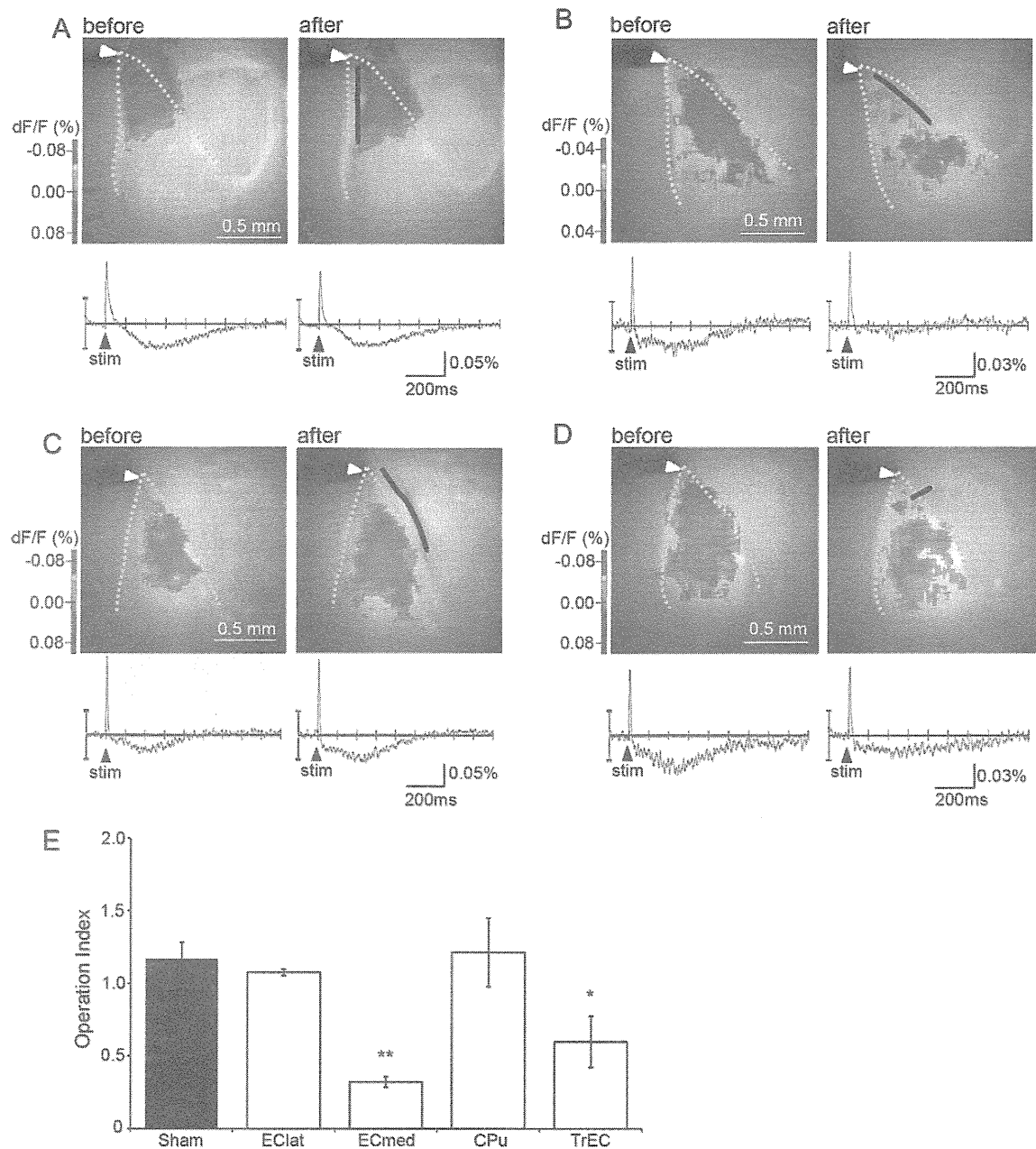
Fig. 2. Effects of deafferentation of the lateral amygdala nucleus on the inhibitory responses.
(A–C) Afferent pathways to the lateral amygdala nucleus were surgically cut from the lateral branch of the external capsule (EClat) in (A), the medial branch (ECmed) in (B), and the caudate putamen (CPu) in (C) to the La was performed, respectively. Black lines, the surgical cut sites; white arrowhead, the stimulating site. The upper images of panels A, B, and C show the spread pattern of hyperpolarization before and after operation. Lower traces, the optical signal traces; black arrowhead, the timing of electrical stimulation. (D) The dorsal part of the ECmed was cut transversely (TrEC). (E) Operation indices (OIs) were quantitatively analyzed among various deafferentations. OIs of ECmed (n = 6 slices from 6 mice) and TrEC (n = 7 slices from 4 mice) were significantly lower than those of Sham (n = 5 slices from 3 mice), EClat (n = 5 slices from 4 mice), and CPu (n = 7 slices from 4 mice). $^*p < 0.05$; $^{**}p < 0.01$.

the stimulation at the other parts (Fig. 3Bd). These results suggest that inhibitory neurons located in the middle part of the ECmed are the main source of the hyperpolarization in the La.

4. Discussion

VSD imaging is a powerful tool to investigate spatial and temporal patterns in the propagation of membrane potential change in the brain tissue. Furthermore, optical signals from the stained slice preparation with VSD are reported to be well-correlated to field EPSPs in vitro [7,8,10,19,25,29,32]. In the amygdala, the

signal propagations from the La to the BLA [35,36] and from the La to the CeA have been visualized using VSD imaging [3]. However, these previous studies focused on the propagation of depolarizing signals in the amygdala but not of hyperpolarizing signals.

In the present study, we demonstrated the propagation of the inhibitory responses in the amygdala formation using VSD imaging. The strong and long-lasting hyperpolarization is evoked in the La after the sharp and strong depolarization. In addition, the surgical-cut and the pharmacological experiments indicate that the source of the inhibitory responses is not located in the La or the CPu, but is located in the middle part of the ECmed. According to this
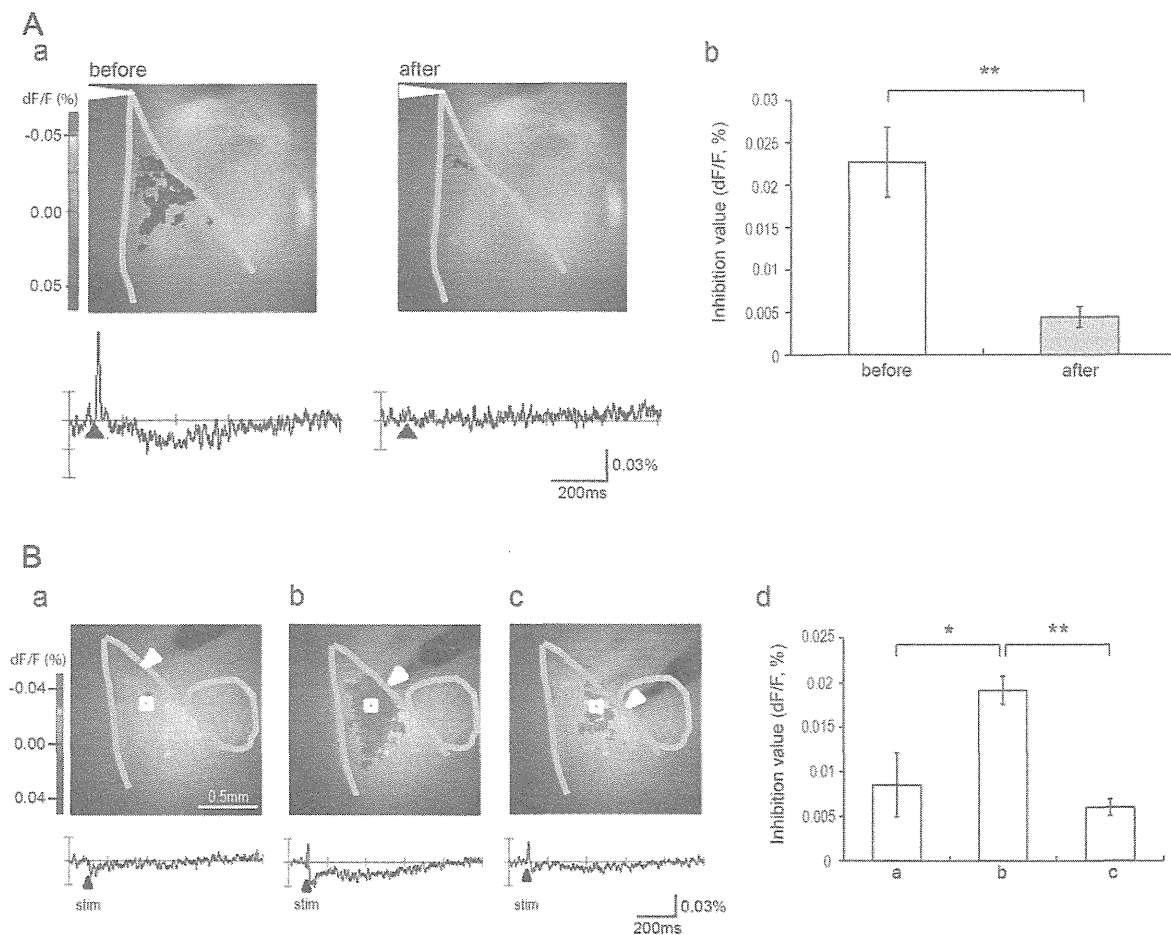
Fig. 3. Effects of glutamatergic antagonists on the inhibitory responses.
(A) The effects of glutamatergic antagonists (CNQX + D-AP5) on the inhibitory response induced by the stimulation of the ramifying point of the external capsule. (Aa) Left and right upper images indicate the spread pattern of hyperpolarization before and after the drug application, respectively. White arrowhead, the stimulating site; lower traces, the optical signal traces; black arrowhead, the timing of electrical stimulation. (Ab) Inhibitory value was statistically compared between before and after CNQX + D-AP5 application ($n = 5$ slices from 5 mice; **$p < 0.01$). (B) The dependence of the stimulus position on inhibitory response of the La in the presence of CNQX + D-AP5. (Ba–c) Upper images indicate the spread pattern of hyperpolarization when the stimulus electrode was at the dorsal, middle, and ventral part of the ECmed, respectively. White arrowhead, the stimulating site; lower traces, the optical signal traces; white squares, the area of which the traces were calculated; black arrowhead, the timing of electrical stimulation. (Bd) Inhibitory value was shown when the stimulus electrode was at the dorsal (a), middle (b), and ventral (c) part of the ECmed ($n = 4$ slices from 4 mice; *$p < 0.05$; **$p < 0.01$).

anatomical location, the source of the inhibitory inputs is likely from the m-ITC in the ECmed [5,18,20,27]. The inhibitory responses were completely eliminated in the presence of the glutamatergic antagonists, indicating that the inhibitory responses are based on the glutamatergic input passing through ECmed. Furthermore, local stimulation of the middle part of the ECmed produces inhibitory responses even in the presence of glutamatergic antagonists, suggesting that GABAergic neurons in the m-ITC are the source of the inhibitory responses of the La. A TrEC cut results in a smaller reduction of the inhibitory responses than an ECmed cut. Because it has been reported that stimulation of the La and the BLA excites the m-ITC neurons [27,28], excitatory glutamatergic inputs to the m-ITC through the La and the BLA might be involved in the inhibitory response in addition to the glutamatergic inputs coming along the ECmed.

In the present study, the contribution of the lateral intercalated clusters located in the EClat was smaller than that of the m-ITC, although the pathway from the lateral intercalated clusters to the BLA has been shown anatomically and electrophysiologically [16,30]. Because the direction of the stimulus electrode used in the present study was from the EClat to the ECmed, resulting in the

selective stimulation of the ECmed, the contribution of the lateral intercalated clusters to the inhibitory response in vivo cannot be excluded.

It has been reported that the stimulation of the La and the BLA excites the m-ITC neurons [27,28], resulting in the inhibition of the CeA neurons [2,27]. This pathway is suggested to be involved in the fear extinction mechanism [1], while the inhibitory inputs from m-ITC to La might interfere with the acquisition of fear memory.

In summary, the present study demonstrates the spatial and temporal spread pattern of the inhibitory response in the La after the stimulation of the EC using VSD imaging. Moreover, it is indicated that the inhibitory response is induced via the m-ITC. The pathway from the m-ITC to the La might have inhibitory effects on the acquisition of fear memory.

Acknowledgements

References

[1] T. Amano, C.T. Unal, D. Pare, Synaptic correlates of fear extinction in the amygdala, Nat. Neurosci. 13 (2010) 489–494.

[2] A. Amir, T. Amano, D. Pare, Physiological identification and infralimbic responsiveness of rat intercalated amygdala neurons, J. Neurophysiol. 105 (2011) 3054–3066.

[3] C. Avrabos, S.V. Sotnikov, J. Dine, P.O. Markt, F. Holsboer, R. Landgraf, M. Eder, Real-time imaging of amygdalar network dynamics in vitro reveals a neurophysiological link to behavior in a mouse model of extremes in trait anxiety, J. Neurosci. 33 (2013) 16262–16267.

[4] E.P. Bauer, J.E. LeDoux, Heterosynaptic long-term potentiation of inhibitory interneurons in the lateral amygdala, J. Neurosci. 24 (2004) 9507–9512.

[5] D. Busti, R. Geracitano, N. Whittle, Y. Dalezios, M. Manko, W. Kaufmann, K. Satzler, N. Singewald, M. Capogna, F. Ferraguti, Different fear states engage distinct networks within the intercalated cell clusters of the amygdala, J. Neurosci. 31 (2011) 5131–5144.

[6] I. Ehrlich, Y. Humeau, F. Grenier, S. Ciocchi, C. Herry, A. Luthi, Amygdala inhibitory circuits and the control of fear memory, Neuron 62 (2009) 757–771.

[7] A. Grinvald, L.B. Cohen, S. Lesher, M.B. Boyle, Simultaneous optical monitoring of activity of many neurons in invertebrate ganglia using a 124-element photodiode array, J. Neurophysiol. 45 (1981) 829–840.

[8] A. Grinvald, A. Manker, M. Segal, Visualization of the spread of electrical activity in rat hippocampal slices by voltage-sensitive optical probes, J. Physiol. 333 (1982) 269–291.

[9] T. Iijima, M.P. Witter, M. Ichikawa, T. Tominaga, R. Kajiwara, G. Matsumoto, Entorhinal-hippocampal interactions revealed by real-time imaging, Science 272 (1996) 1176–1179.

[10] W. Jin, R.J. Zhang, J.Y. Wu, Voltage-sensitive dye imaging of population neuronal activity in cortical tissue, J. Neurosci. Methods 115 (2002) 13–27.

[11] M.Z. Kee, J.P. Wuskell, L.M. Loew, G.J. Augustine, Y. Sekino, Imaging activity of neuronal populations with new long-wavelength voltage-sensitive dyes, Brain Cell Biol. 36 (2008) 157–172.

[12] N. Koganezawa, A. Taguchi, T. Tominaga, S. Ohara, K. Tsutsui, M.P. Witter, T. Iijima, Significance of the deep layers of entorhinal cortex for transfer of both perirhinal and amygdala inputs to the hippocampus, Neurosci. Res. 61 (2008) 172–181.

[13] J.E. LeDoux, Emotion circuits in the brain, Annu. Rev. Neurosci. 23 (2000) 155–184.

[14] J.E. LeDoux, P. Cicchetti, A. Xagoraris, L.M. Romanski, The lateral amygdaloid nucleus: sensory interface of the amygdala in fear conditioning, J. Neurosci. 10 (1990) 1062–1069.

[15] D. Marcellino, M. Frankowska, L. Agnati, M. Perez de la Mora, V. Vargas-Barroso, K. Fuxe, J. Larriva-Sahd, Intercalated and paracapsular cell islands of the adult rat amygdala: a combined rapid-Golgi, ultrastructural, and immunohistochemical account, Neuroscience 226 (2012) 324–347.

[16] A. Marowsky, Y. Yanagawa, K. Obata, K.E. Vogt, A specialized subclass of interneurons mediates dopaminergic facilitation of amygdala function, Neuron 48 (2005) 1025–1037.

[17] A.J. McDonald, Neurons of the lateral and basolateral amygdaloid nuclei: a Golgi study in the rat, J. Comp. Neurol. 212 (1982) 293–312.

[18] O.E. Millhouse, The intercalated cells of the amygdala, J. Comp. Neurol. 247 (1986) 246–271.

[19] M. Nakamura, Y. Sekino, T. Manabe, GABAergic interneurons facilitate mossy fiber excitability in the developing hippocampus, J. Neurosci. 27 (2007) 1365–1373.

[20] L. Nitecka, Y. Ben-Ari, Distribution of GABA-like immunoreactivity in the rat amygdaloid complex, J. Comp. Neurol. 266 (1987) 45–55.

[21] H.C. Pape, D. Pare, Plastic synaptic networks of the amygdala for the acquisition, expression, and extinction of conditioned fear, Physiol. Rev. 90 (2010) 419–463.

[22] D. Pare, G.J. Quirk, J.E. Ledoux, New vistas on amygdala networks in conditioned fear, J. Neurophysiol. 92 (2004) 1–9.

[23] D. Pare, Y. Smith, Distribution of GABA immunoreactivity in the amygdaloid complex of the cat, Neuroscience 57 (1993) 1061–1076.

[24] D. Pare, Y. Smith, The intercalated cell masses project to the central and medial nuclei of the amygdala in cats, Neuroscience 57 (1993) 1077–1090.

[25] D. Plenz, A. Aertsen, Current source density profiles of optical recording maps: a new approach to the analysis of spatio-temporal neural activity patterns, Eur. J. Neurosci. 5 (1993) 437–448.

[26] D.G. Rainnie, E.K. Asprodini, P. Shinnick-Gallagher, Inhibitory transmission in the basolateral amygdala, J. Neurophysiol. 66 (1991) 999–1009.

[27] S. Royer, M. Martina, D. Pare, An inhibitory interface gates impulse traffic between the input and output stations of the amygdala, J. Neurosci. 19 (1999) 10575–10583.

[28] S. Royer, M. Martina, D. Pare, Polarized synaptic interactions between intercalated neurons of the amygdala, J. Neurophysiol. 83 (2000) 3509–3518.

[29] Y. Sekino, K. Obata, M. Tanifuji, M. Mizuno, J. Murayama, Delayed signal propagation via CA2 in rat hippocampal slices revealed by optical recording, J. Neurophysiol. 78 (1997) 1662–1668.

[30] Y. Silberman, L. Shi, J.K. Brunso-Bechtold, J.L. Weiner, Distinct mechanisms of ethanol potentiation of local and paracapsular GABAergic synapses in the rat basolateral amygdala, J. Pharmacol. Exp. Ther. 324 (2008) 251–260.

[31] C. Szinyei, T. Heinbockel, J. Montagne, H.C. Pape, Putative cortical and thalamic inputs elicit convergent excitation in a population of GABAergic interneurons of the lateral amygdala, J. Neurosci. 20 (2000) 8909–8915.

[32] T. Tominaga, Y. Tominaga, H. Yamada, G. Matsumoto, M. Ichikawa, Quantification of optical signals with electrophysiological signals in neural activities of Di-4-ANEPPS stained rat hippocampal slices, J. Neurosci. Methods 102 (2000) 11–23.

[33] Y. Tominaga, M. Ichikawa, T. Tominaga, Membrane potential response profiles of CA1 pyramidal cells probed with voltage-sensitive dye optical imaging in rat hippocampal slices reveal the impact of GABA(A)-mediated feed-forward inhibition in signal propagation, Neurosci. Res. 64 (2009) 152–161.

[34] S. Tsuda, M.Z. Kee, C. Cunha, J. Kim, P. Yan, L.M. Loew, G.J. Augustine, Probing the function of neuronal populations: combining micromirror-based optogenetic photostimulation with voltage-sensitive dye imaging, Neurosci. Res. 75 (2013) 76–81.

[35] C. Wang, M.H. Kang-Park, W.A. Wilson, S.D. Moore, Properties of the pathways from the lateral amygdal nucleus to basolateral nucleus and amygdalostriatal transition area, J. Neurophysiol. 87 (2002) 2593–2601.

[36] C. Wang, W.A. Wilson, S.D. Moore, Role of NMDA, non-NMDA, and GABA receptors in signal propagation in the amygdala formation, J. Neurophysiol. 86 (2001) 1422–1429.

[37] A.R. Woodruff, H. Monyer, P. Sah, GABAergic excitation in the basolateral amygdala, J. Neurosci. 26 (2006) 11881–11887.

[38] A.R. Woodruff, P. Sah, Networks of parvalbumin-positive interneurons in the basolateral amygdala, J. Neurosci. 27 (2007) 553–563.

Short communication

Paroxetine prevented the down-regulation of astrocytic L-Glu transporters in neuroinflammation

CrossMark

Koki Fujimori [a, b], Junpei Takaki [a, b], Yukari Shigemoto-Mogami [a], Yuko Sekino [a], Takeshi Suzuki [b], Kaoru Sato [a, *]

[a] Laboratory of Neuropharmacology, Division of Pharmacology, National Institute of Health Sciences, 1-18-1 Kamiyoga, Setagaya-ku, Tokyo 158-8501, Japan
[b] Division of Basic Biological Science, Faculty of Pharmacy, Keio University, 1-5-30 Shiba-koen, Minato-ku, Tokyo 105-8512, Japan

ARTICLE INFO

ABSTRACT

The extracellular L-glutamate (L-Glu) concentration is elevated in neuroinflammation, thereby causing excitotoxicity. One of the mechanisms is down-regulation of astrocyte L-Glu transporters. Some antidepressants have anti-inflammatory effects. We therefore investigated effects of various antidepressants on the down-regulation of astrocyte L-Glu transporters in the in vitro neuroinflammation model. Among these antidepressants, only paroxetine was effective. We previously demonstrated that the down-regulation of astrocyte L-Glu transporters was caused by L-Glu released from activated microglia. We here clarified that only paroxetine inhibited L-Glu release from microglia. This is the novel action of paroxetine, which may bring advantages on the therapy of neuroinflammation.
© 2014 Japanese Pharmacological Society. Production and hosting by Elsevier B.V. This is an open access article under the CC BY-NC-ND license (http://creativecommons.org/licenses/by-nc-nd/4.0/).

Increasing evidence indicates that inflammatory processes play important roles in the pathogenesis of many neurodegenerative disorders (1–3). Under the neuroinflammatory conditions, it is known that the extracellular concentration of L-glutamate (L-Glu) and inflammatory mediators, such as proinflammatory cytokines, prostaglandins, free radicals and complements are elevated (4). L-Glu is one of the most abundant excitatory neurotransmitters in the mammalian CNS. The released L-Glu is immediately uptaken by astrocyte L-Glu transporters, GLAST (EAAT1 in human) and GLT-1 (EAAT2 in human), or sustained elevation of extracellular concentration of L-Glu induce excitotoxicity. The impairment of the astrocyte L-Glu transporters is reported in various neurological disorders including Alzheimer's disease (5), Parkinson's diseases (6) and amyotrophic lateral sclerosis (7). We found that the expression level of L-Glu transporters in astrocytes of astrocyte-microglia-neuron mixed culture was decreased in the in vitro model of the early stage of inflammation in the previous study (8). We clarified the interaction between astrocytes and microglia underlie the down-regulation of L-Glu transporters, i.e., activated microglia release L-Glu and the resulting elevation of extracellular L-Glu cause down-regulation of astrocytic L-Glu transporters. Some antidepressants are known to have anti-inflammatory effects (9, 10). In this study, therefore, we investigated the effects of various antidepressants on the decrease in the astrocytic L-Glu transporter function in the early stage of inflammation and the contribution of microglia to the effects.

Astrocyte-microglia-neuron mixed culture and microglia culture were performed according to the methods previously described (8). Antidepressants and serotonin (5-HT) were dissolved in PBS at 100 μM and 10 mM, respectively, and were diluted with culture medium at the time of use. At 8 DIV, the astrocyte-microglia-neuron mixed culture was treated with 10 ng/mL LPS for 72 h. Antidepressants were applied from 1 h before to the end of the LPS-treatment. Then the concentration of the L-Glu remaining in the culture medium 30 min after changing extracellular concentration of L-Glu to 100 μM was measured. The measurement of the extracellular L-Glu concentration in the medium was performed according to the methods previously described (8). Real-Time Quantitative RT-PCR, Western blotting, immunocytochemistry were also performed according to the methods previously
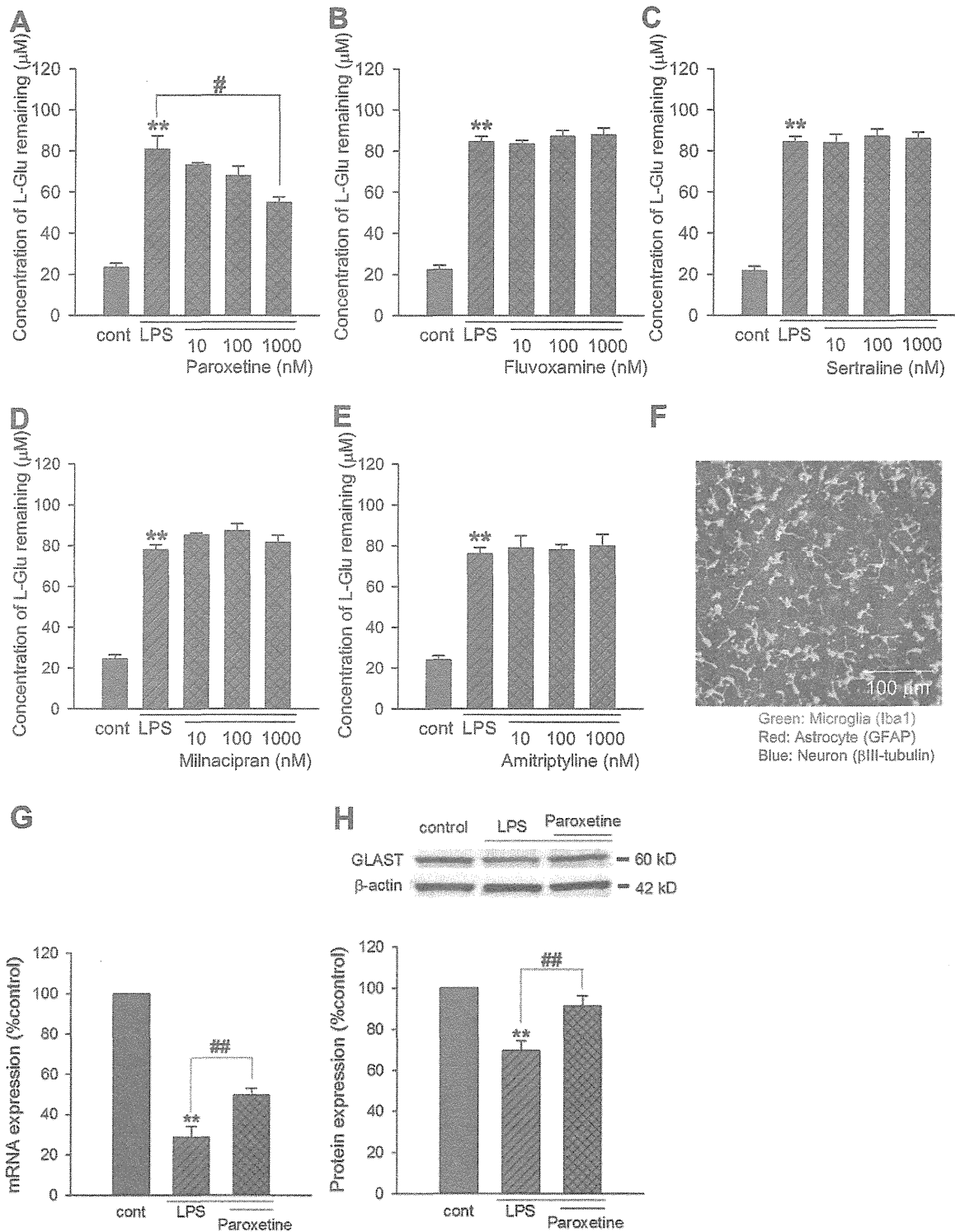
Fig. 1. Effects of antidepressants on the decreased L-Glu transport activity under the inflammatory condition. A–E. Antidepressants were applied to the mixed culture from 1 h before to the end of the LPS-treatment (10 ng/ml, 72 h). L-Glu transport activity was quantified as the L-Glu remaining 30 min after changing the extracellular concentration to 100 μM. Paroxetine prevented the LPS-induced decrease in the L-Glu transport activity in a concentration-dependent manner (A). Fluvoxamine (B), sertraline (C), milnacipran (D), and amitriptyline (E) had no effects. **: $p < 0.01$ vs. control group, #: $p < 0.05$ vs. LPS-treated group, Tukey's test following ANOVA ($N = 6$). F. Typical image of the microglia-astrocyte-neuron mixed culture immunostained with cell type-specific markers (Iba1: microglia; GFAP: astrocytes; βIII tubulin: neurons). G, H. Effects of paroxetine on the expression level of GLAST. Mixed cultures were treated with LPS (10 ng/ml) in the absence or presence of the paroxetine for 24 h (for mRNA level quantification) or 72 h (for protein level quantification). The expression level of GLAST was quantified at mRNA level (G) and protein level (H). LPS (10 ng/ml) caused significant decrease in GLAST mRNA level and paroxetine significantly prevented the decrease (G). LPS (10 ng/ml) caused significant decrease in GLAST protein level and paroxetine almost completely prevented the decrease (H). **: $p < 0.01$ vs. control group, ##: $p < 0.01$ vs. LPS-treated group, Tukey's test following ANOVA ($N = 5$).

described (8). The microglia culture was treated with LPS for 24 h in the presence or absence of antidepressants and the concentration of L-Glu in the medium was measured. All sets of the experiments were repeated in triplicate. All procedures described above were in accordance with institutional guidelines.

In the previous report, we showed that the expression level of astrocytic L-Glu transporters was decreased in the astrocyte-microglia-neuron mixed culture in LPS (10 ng/ml, 72 h)-induced inflammation model without cell death (8). We first compared the effects of various groups of antidepressants, i.e., selective serotonin reuptake inhibitors (SSRIs) (paroxetine, fluvoxamine, and sertraline), serotonin–norepinephrine reuptake inhibitor (SNRI) (milnacipran), and tricyclic antidepressant (TCA) (amitriptyline), on the decrease in the astrocytic L-Glu transporter function in this inflammation model. To quantify L-Glu transport activity, we measured the concentration of L-Glu remaining 30 min after changing the medium to the one containing 100 μM of L-Glu. In each set of experiment, LPS-induced decrease in the L-Glu transport

activity was stably reproduced (Fig. 1A–E). Among antidepressants, only paroxetine prevented the LPS-induced decrease in L-Glu transport activity (Fig. 1A). The effect was concentration-dependent and reached significant at 1 μM. The other antidepressants had no effects (Fig. 1B–E). Typical image of the astrocyte-microglia-neuron mixed culture was shown in Fig. 1F. We have clarified that LPS-induced decrease in L-Glu transport activity was caused by the decrease in the expression level of GLAST, a predominant L-Glu transporter in the mixed culture, in both of mRNA and protein levels (8). In this study, LPS-induced decreases in the expression of GLAST, were reproduced at both of mRNA ($28.8 \pm 4.7\%$ of the control) and protein ($69.5 \pm 4.7\%$ of the control) levels (Fig. 1G, H). We then examined the effects of paroxetine on the LPS-induced decrease in the L-Glu transporter expression. Paroxetine significantly prevented the decreases at both of mRNA (28.8 ± 4.7 to $49.6 \pm 3.3\%$; $n = 10$) and protein (from $69.5 \pm 4.7\%$ to $91.0 \pm 5.1\%$; $n = 5$) levels (Fig. 1G, H). As is shown in Fig. 1, fluvoxamine and sertraline, the other SSRIs in this study, did not affect the decrease in L-Glu transport activity, suggesting that paroxetine revealed the effects through the mechanisms independent of its inhibitory effect on serotonin selective transporter. In support of this, LPS-induced decrease in L-Glu transport activity was not changed by the elevation of extracellular serotonin concentration (Fig. 2A). We also confirmed that paroxetine did not directly affect the L-Glu transport activity of the astrocyte culture (Fig. 2B). In our previous report, the down-regulation of GLAST in the inflammation model was caused by the elevation of extracellular L-Glu released from microglia (8). We therefore compared the effects of the antidepressants on LPS-induced L-Glu release from microglia. When microglia culture was treated with 10 ng/ml LPS for 24 h in the presence or absence of the antidepressants, only paroxetine suppressed L-Glu release in a concentration-dependent manner (Fig. 3A). The other antidepressants had no effects (Fig. 3B–E). We confirmed that paroxetine did not affect the microglial viability until 10 μM by LDH assay (data not shown). These results strongly suggest that the protective effect of paroxetine on the LPS-induced down-regulation of astrocytic L-Glu transporters was caused by the suppression of L-Glu release from microglia.

The shape of microglia in the mixed culture was dramatically changed to amoeboid type by LPS and this morphological change was remarkably suppressed by paroxetine (unpublished observation). This suggests that paroxetine does not only suppress L-Glu release from microglia alone but also microglial activation. To demonstrate this possibility, the effect of paroxetine on the microglial activation is needed to be confirmed using multiple parameters. Because SSRIs have diverse chemical structures despite a common mode of action of 5-HT function (11), it is possible that paroxetine revealed the effects through interaction with paroxetine-specific target molecules. Because paroxetine exhibited the powerful inhibition of calcium influx via P2X$_4$ receptors (12), P2X$_4$ receptor is one of the most probable candidate molecules. The expression level of P2X$_4$ receptor in microglia is up-regulated in inflammatory pain model in spinal cord and is thought to be important for microglial inflammatory responses (13). MAPK signaling molecules (14) and GABA(B) receptor (15) are possibly involved in the paroxetine-specific effects as well. The effective concentration of paroxetine to reduce L-Glu release was 1 μM. According to the attached documents of paroxetine (http://www.info.pmda.go.jp/), intracerebral concentration of paroxetine reaches 77 nM by 25 mg/day-repeated administration. It is therefore unlikely that paroxetine affects astrocyte L-Glu transporters and microglia by the general dosage of SSRI. For clinical application of our present findings, further investigation concerning application period and dosage is needed.
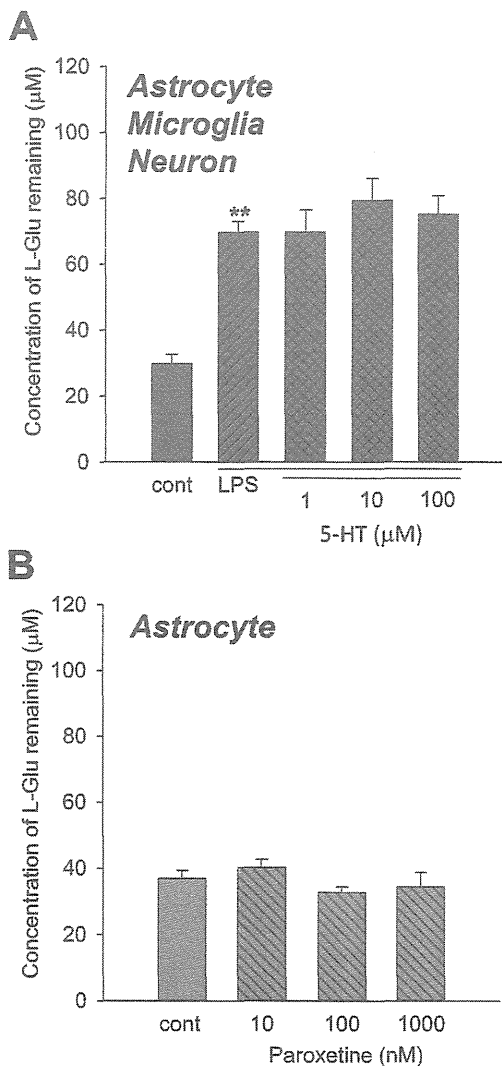
Fig. 2. Relation of the effects of paroxetine on LPS-induced decrease in L-Glu transport activity with its SSRI function and the direct effect on astrocytes. A. 72 h treatment with 5-HT (1–100 μM) did not affect LPS-induced decrease in the L-Glu transport activity. B. 72 h treatment with paroxetine (10–1000 nM) of astrocyte culture did not affect its L-Glu transport activity. **: $p < 0.01$ vs. control group, Tukey's test following ANOVA ($N = 6$).
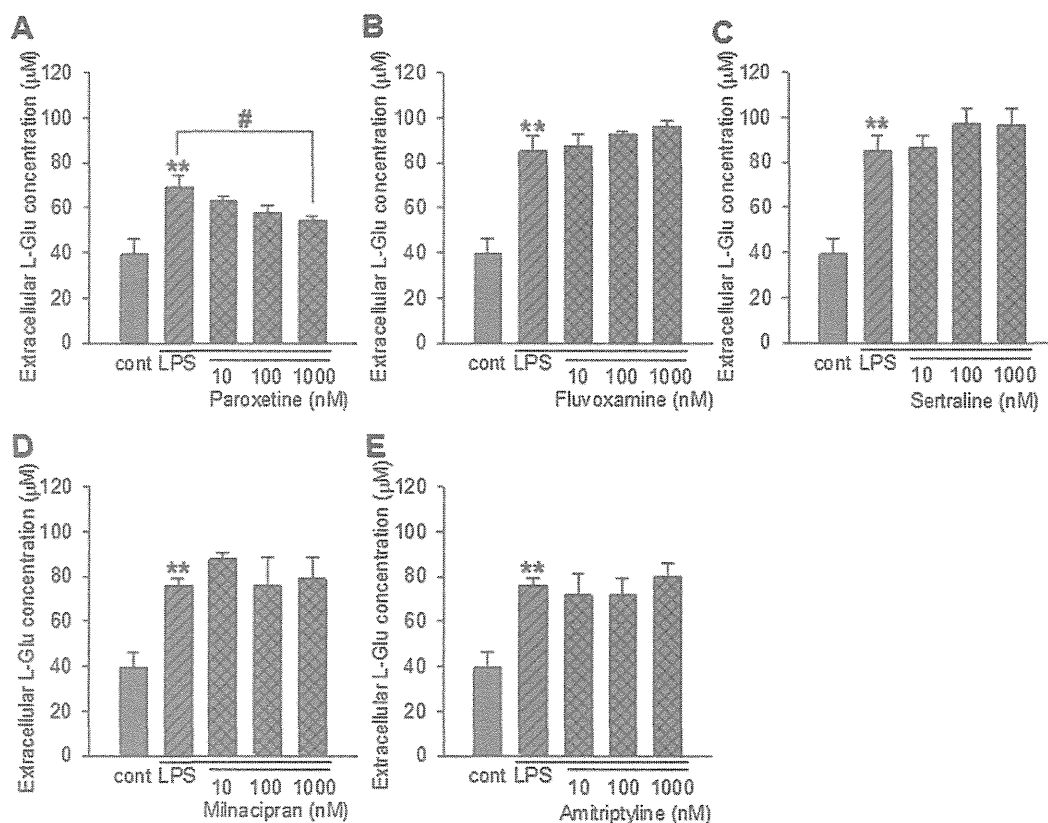
Fig. 3. Effects of antidepressants on the L-Glu release from microglia under the inflammatory condition. In each set of experiment, antidepressants were applied to the mixed culture from 1 h before to the end of the LPS-treatment (10 ng/ml, 24 h). The extracellular concentration of L-Glu was quantified. Paroxetine prevented the LPS-induced L-Glu release from microglia in a concentration-dependent manner (A). Fluvoxamine (B), sertraline (C), milnacipran (D), and amitriptyline (E) had no effects on LPS-induced L-Glu release from microglia. **: $p < 0.01$ vs. control group, #: $p < 0.05$ vs. LPS-treated group, Tukey's test following ANOVA ($N = 6$).

In conclusion, we found that paroxetine inhibit the L-Glu release from activated microglia and prevent down-regulation of astrocytic L-Glu transporters in the early stage of neuroinflammation. This is the novel pharmacological effect of paroxetine, which may bring advantages on the therapy of the disease associated with neuroinflammation.

Conflicts of interest

I declare that I have no significant competing financial, professional or personal interests that might have influenced the results and interpretation of the manuscript.

Author's contributions

K.F. performed experiments and manuscript writing.

J.T. performed experiments.

Y.S-M. provided advice on manuscript writing

Y.S. provided advice on manuscript writing

T.S. provided advice on the experimental direction and manuscript writing.

K.S. designed the experimental plan and performed experiments, manuscript writing.

Acknowledgments

References

(1) Bowerman M, Vincent T, Scamps F, Perrin FE, Camu W, Raoul C. Neuro-immunity dynamics and the development of therapeutic strategies for amyotrophic lateral sclerosis. Front Cell Neurosci. 2013;7:214.
(2) Liimatainen S, Lehtimaki K, Palmio J, Alapirtti T, Peltola J. Immunological perspectives of temporal lobe seizures. J Neuroimmunol. 2013;263:1–7.
(3) Schwartz M, Baruch K. The resolution of neuroinflammation in neuro-degeneration: leukocyte recruitment via the choroid plexus. EMBO J. 2014;33: 7–22.
(4) Lucas SM, Rothwell NJ, Gibson RM. The role of inflammation in CNS injury and disease. Br J Pharmacol. 2006;147(Suppl. 1):S232–S240.
(5) Masliah E, Alford M, DeTeresa R, Mallory M, Hansen L. Deficient glutamate transport is associated with neurodegeneration in Alzheimer's disease. Ann Neurol. 1996;40:759–766.
(6) Ferrarese C, Zoia C, Pecora N, Piolti R, Frigo M, Bianchi G, et al. Reduced platelet glutamate uptake in Parkinson's disease. J Neural Transm. 1999;106: 685–692.
(7) Rothstein JD, Martin LJ, Kuncl RW. Decreased glutamate transport by the brain and spinal cord in amyotrophic lateral sclerosis. N Engl J Med. 1992;326: 1464–1468.
(8) Takaki J, Fujimori K, Miura M, Suzuki T, Sekino Y, Sato K. L-glutamate released from activated microglia downregulates astrocytic L-glutamate transporter

expression in neuroinflammation: the 'collusion' hypothesis for increased extracellular L-glutamate concentration in neuroinflammation. J Neuroinflammation. 2012;9:275.

(9) Hashioka S, Klegeris A, Monji A, Kato T, Sawada M, McGeer PL. et al. Antidepressants inhibit interferon-gamma-induced microglial production of IL-6 and nitric oxide. Exp Neurol. 2007;206:33–42.

(10) Hwang J, Zheng LT, Ock J, Lee MG, Kim SH, Lee HW, et al. Inhibition of glial inflammatory activation and neurotoxicity by tricyclic antidepressants. Neuropharmacology. 2008;55:826–834.

(11) RJ B. Drugs and the treatment of psychiatrc disorders. Goodman and Gilman's the pharmacological basis of therapeutics. In: Hardman JG, Limbird LE, Gilman AG, editors. 10th ed 2001. p. 447–483.

(12) Nagata K, Imai T, Yamashita T, Tsuda M, Tozaki-Saitoh H, Inoue K. Antidepressants inhibit P2X4 receptor function: a possible involvement in neuropathic pain relief. Mol Pain. 2009;5:20.

(13) Guo LH, Trautmann K, Schluesener HJ. Expression of P2X4 receptor by lesional activated microglia during formalin-induced inflammatory pain. J Neuroimmunol. 2005;163:120–127.

(14) Liu RP, Zou M, Wang JY, Zhu JJ, Lai JM, Zhou LL, et al. Paroxetine ameliorates lipopolysaccharide-induced microglia activation via differential regulation of MAPK signaling. J Neuroinflammation. 2014;11:47.

(15) Khundakar AA, Zetterstrom TS. Effects of GABAB ligands alone and in combination with paroxetine on hippocampal BDNF gene expression. Eur J Pharmacol. 2011;671:33–38.

SHORT COMMUNICATION

Evaluation of the neurochemical effects of methoxetamine using brain microdialysis in mice

Yuki Fuchigami · Xunsing Fu · Rie Ikeda · Shigeru Kawakami ·
Mitsuhiro Wada · Ruri Kikura-Hanajiri · Naotaka Kuroda ·
Kenichiro Nakashima

Abstract The ketamine analogue, 2-(3-methoxyphenyl)-2-(ethylamino)cyclohexanone (methoxetamine) has emerged as a drug of abuse. Both methoxetamine and ketamine are antagonists of glutamate N-methyl-D-asparate receptors, and several case reports show that methoxetamine produces similar schizophrenia-like symptoms and hallucinations to ketamine. Although methoxetamine is believed to change levels of dopamine, glutamate, and serotonin in the brain, few studies thus far have examined these effects. We investigated the influence of methoxetamine on dopamine and serotonin concentrations using microdialysis and high performance liquid chromatography with electrochemical detection. To reveal the effects of methoxetamine, we monitored dopamine and serotonin concentrations in several brain areas [striatum, nucleus accumbens, and prefrontal cortex (mPFC)] after an administration of 20 mg/kg of methoxetamine. We compared the effects of methoxetamine with those of ketamine using two ketamine doses. Methoxetamine increased dopamine and serotonin concentrations most robustly in the mPFC. In addition, its effects were stronger than those of ketamine at the same molar dose, suggesting that methoxetamine causes schizophrenia-like symptoms and hallucinations by increasing the dopamine and serotonin concentrations. We conclude that consumption of methoxetamine may be more dangerous than consumption of ketamine.

Keywords Methoxetamine · Ketamine · Dopamine · Serotonin · Prefrontal cortex · NMDA receptor antagonist

Introduction

Drug abuse is a serious issue worldwide, and now affects a wide age range of individuals, including teenagers, and results in traffic accidents, mental or physical morbidity, and death [1, 2]. Although a number of countries have managed to eradicate some drugs, drug abuse continues because of insufficient guidance on the associated risks and easy access via the Internet. Therefore, scientific or clinical evidence that demonstrates the risks of these drugs is urgently needed to prevent harmful drug abuse.

The ketamine analogue, 2-(3-methoxyphenyl)-2-(ethylamino)cyclohexanone (methoxetamine) has emerged as a novel drug of abuse [3, 4]. Methoxetamine and ketamine are classified as N-methyl-D-asparate (NMDA) receptor antagonists [5] in a class that includes diclofensine [6], diphenidine [6, 7], and phencyclidine [7]. Several case reports show that methoxetamine has a variety of pharmacological effects, side effects, and physical symptoms similar to ketamine, such as euphoria, hallucinations, and schizophrenia-like symptoms [3, 4, 8, 9]. In addition, the N-ethyl group of methoxetamine is considered to engender its stronger pharmacological effects compared with ketamine [4], and abusers of methoxetamine report that the

Y. Fuchigami · X. Fu · R. Ikeda · S. Kawakami · N. Kuroda
Graduate School of Biomedical Sciences, Nagasaki University,
Nagasaki 852-8521, Japan

M. Wada (✉)
School of Pharmaceutical Sciences, Kyusyu University of Health
and Welfare, 1714-1 Yoshino-cho,
Nobeoka, Miyazaki 882-8508, Japan
e-mail: m-wada@phoenix.ac.jp

R. Kikura-Hanajiri
National Institute of Health Sciences, Tokyo 158-8501, Japan

K. Nakashima
Faculty of Pharmaceutical Sciences, Nagasaki International
University, Sasebo, Nagasaki 859-3298, Japan

⌐ Springer